Supplementary information

Nitrogen/oxygen/sulfur tri-doped hard carbon nanospheres derived from waste tires with high sodium and potassium anodic performances

Qian Zhao,[a,b,c,1] Qiaotian Zheng,[a,1] Shenghu Li,[a] Bin He,[a] Xiulong Wu,[a] Yujue Wang,[c] Qingyuan Wang,[a,c] Yan Meng,[d] * and Dan Xiao,[c,d] *

[a] *College of Mechanical Engineering, Chengdu University, No. 2025, Chengluo Road, Chengdu 610106, PR China.*

[b] *Solid-state Fermentation Resource Utilization Key Laboratory of Sichuan Province, Yibin University, No. 8, Jiusheng Road, Yibin 644000, PR China.*

[c] *Institute for Advanced Study, Chengdu University, Chengdu 610106, PR China.*

[d] *Institute of New Energy and Low-Carbon Technology, Sichuan University, Chengdu 610065, PR China.*

---

* Corresponding authors. E-mail address: meng.yan.scu@hotmail.com (Y. Meng), xiaodan@scu.edu.cn (D. Xiao).

[1] These authors contributed equally to this work.

XPS etching: Al Kα microfocusing monochromatic source was adopted for XPS etching, and CAE scanning mode was used to achieve high-performance data acquisition with low power consumption (72 W). The vacuum degree of the analysis room is ≤ 2×10^{-7} mbar. Full spectrum scanning was performed with a flux of 100 eV and a step size of 1 eV, and narrow-spectrum scanning was performed with a pass energy of 30 to 50 eV and a step size of 0.05 to 0.1 eV. The number of scans was adjusted 5-20 times in combination with the pass, step size and signal strength. C1s (284.8 eV) was used as the standard for binding energy correction.

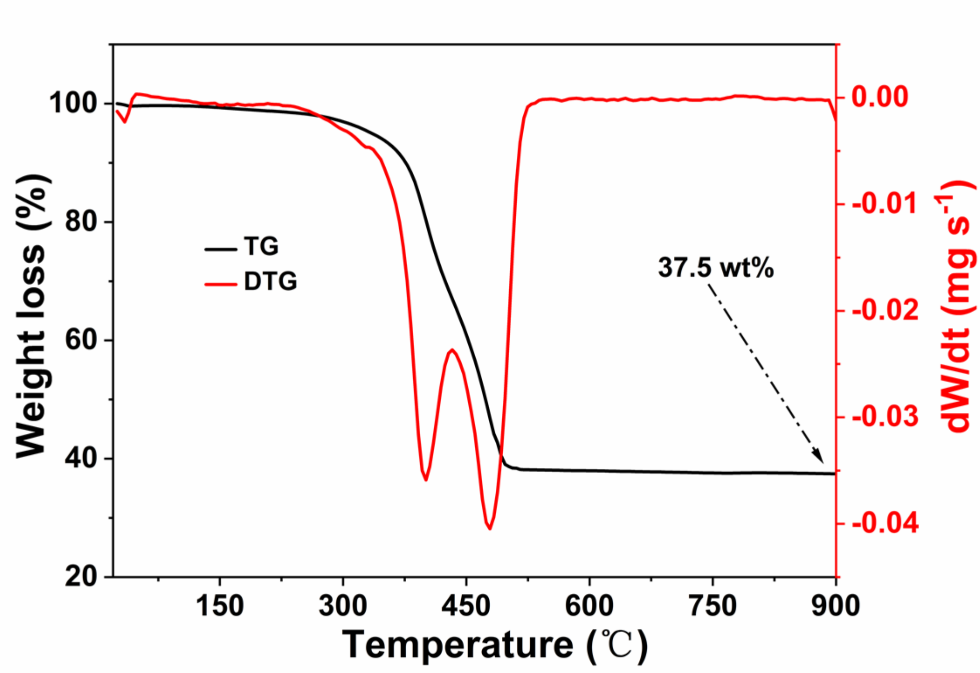

Fig. S1 TG curve of the waste tires pyrolyzed in argon at a heating rate of 5 °C min^{-1}.

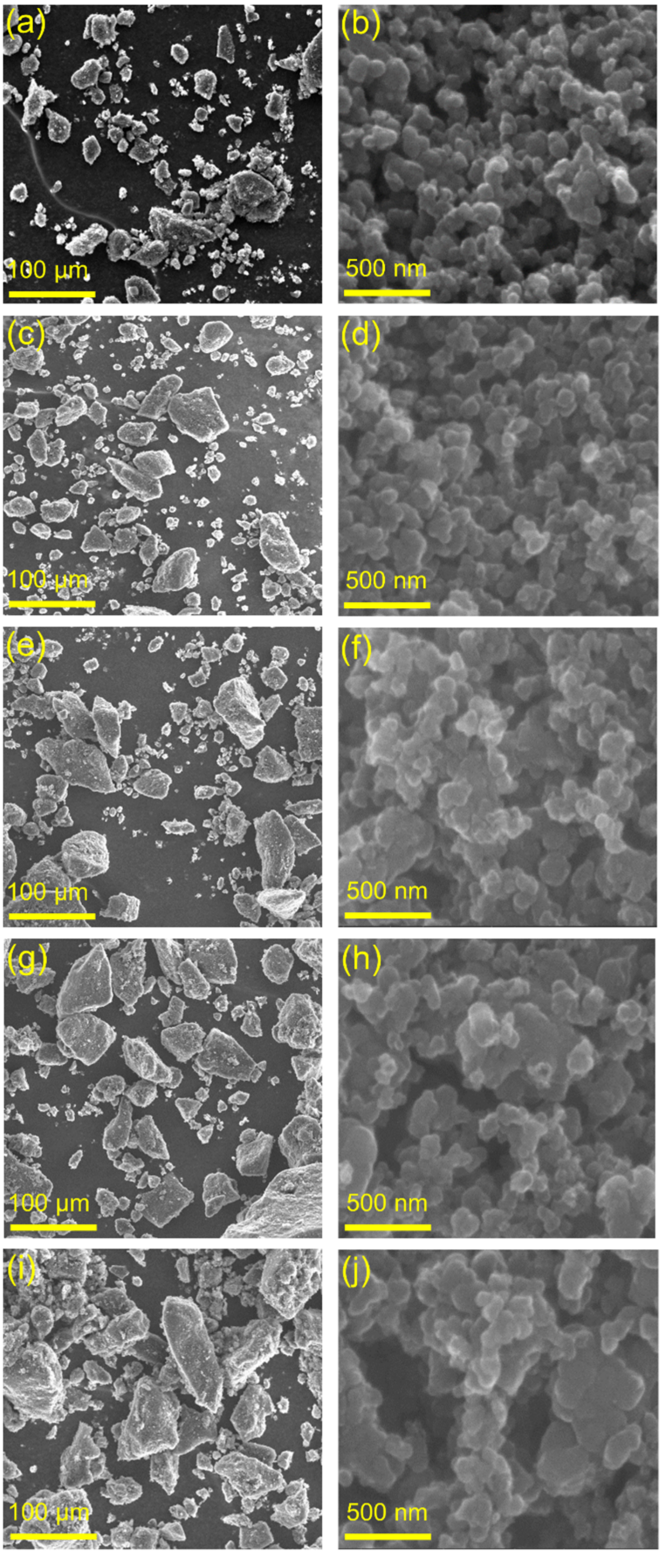

Fig. S2 The SEM images of NOS-HCs. (a, b) NOS-HC700, (c, d) NOS-HC800, (e, f) NOS-HC900, (g, h) NOS-HC1000 and (i, j) NOS-HC1100.

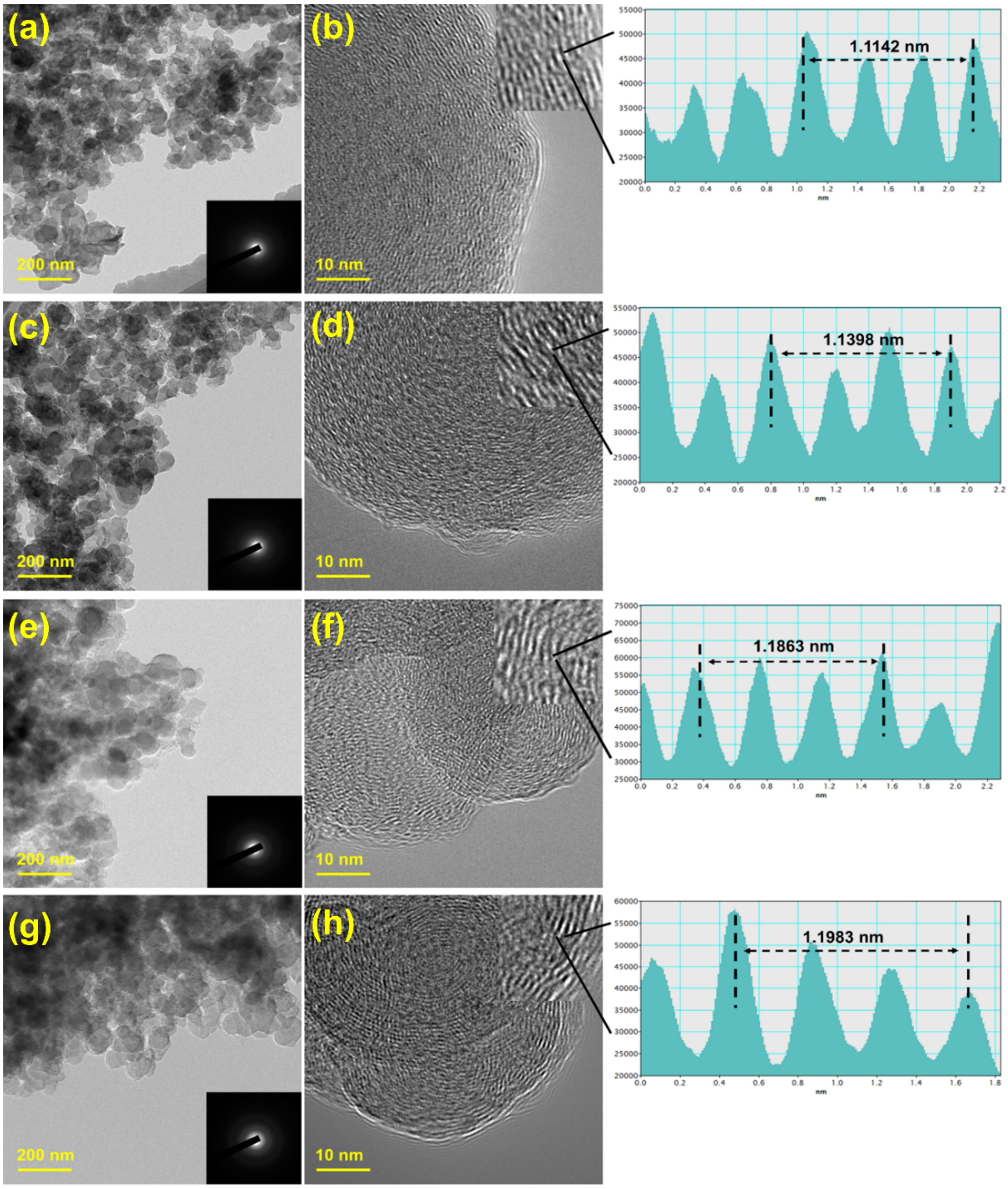

Fig. S3 The TEM images and lattice fringes (insets) of NOS-HCs: (a, b) NOS-HC700, (c, d) NOS-HC800, (e, f) NOS-HC1000 and (g, h) NOS-HC1100.

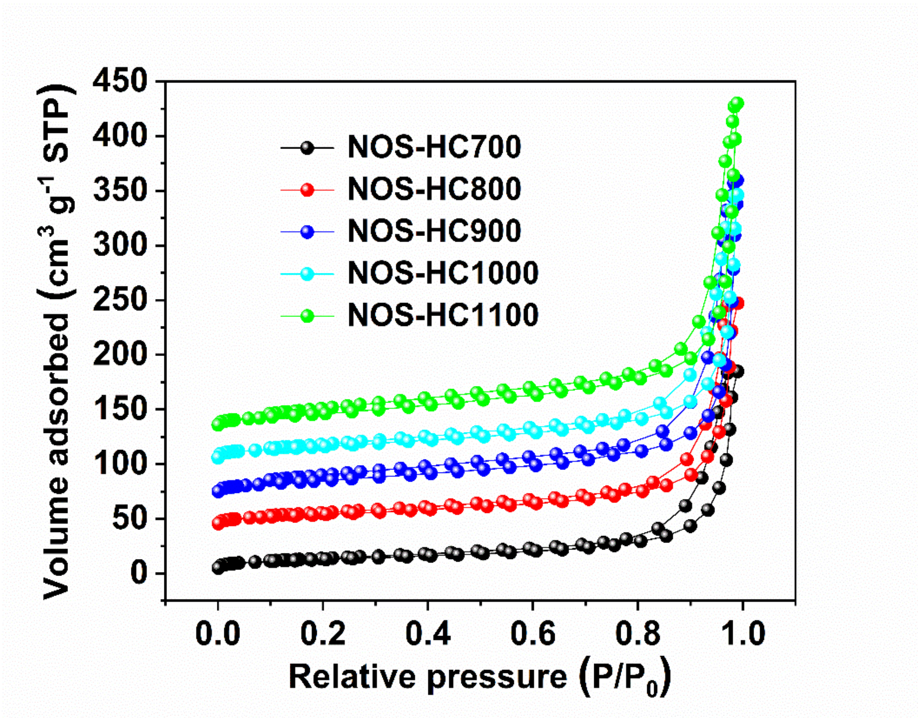

Fig. S4 The N_2 adsorption-desorption isotherms curves.

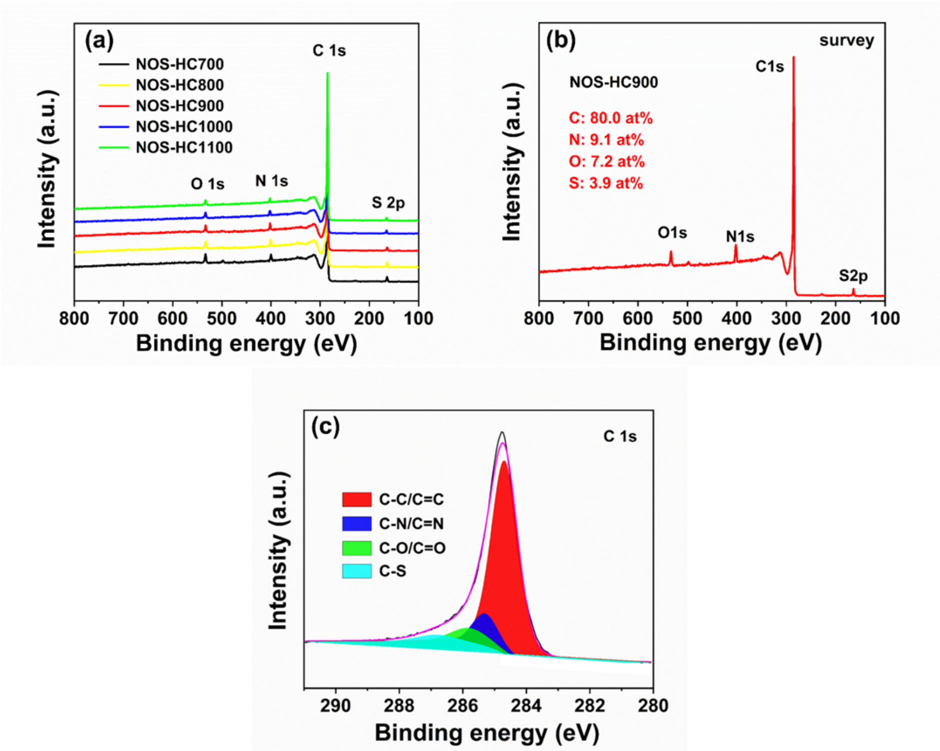

Fig. S5 XPS survey spectrums of the NOS-HCs, (b) the survey spectra and chemical composition of NOS-HC900 and (c) the C 1s spectrum.

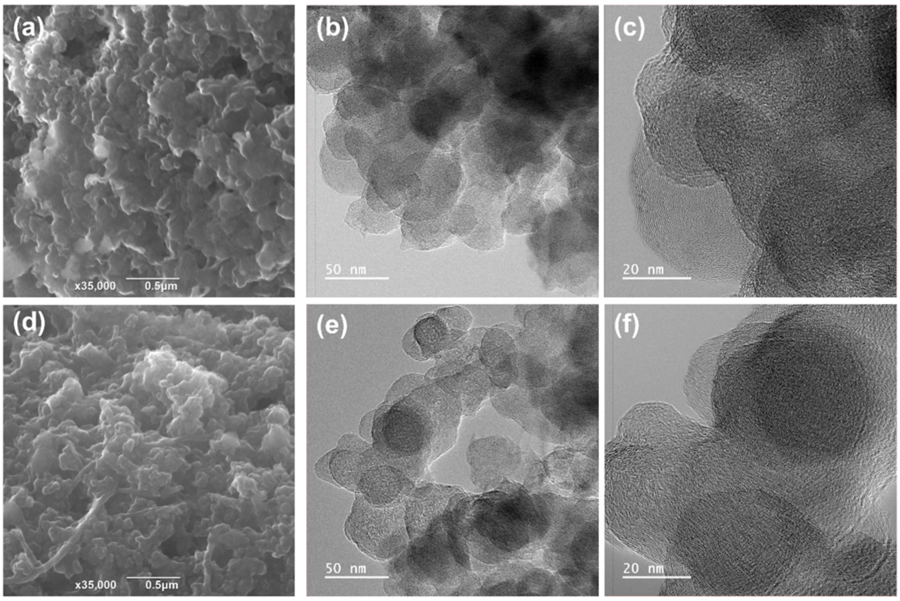

Fig. S6 The microstructure of NOS-HC900 with after cycling: the SEM image of SIBs (a) and PIBs (b), the TEM image of SIBs (b, c) and PIBs (e, f).

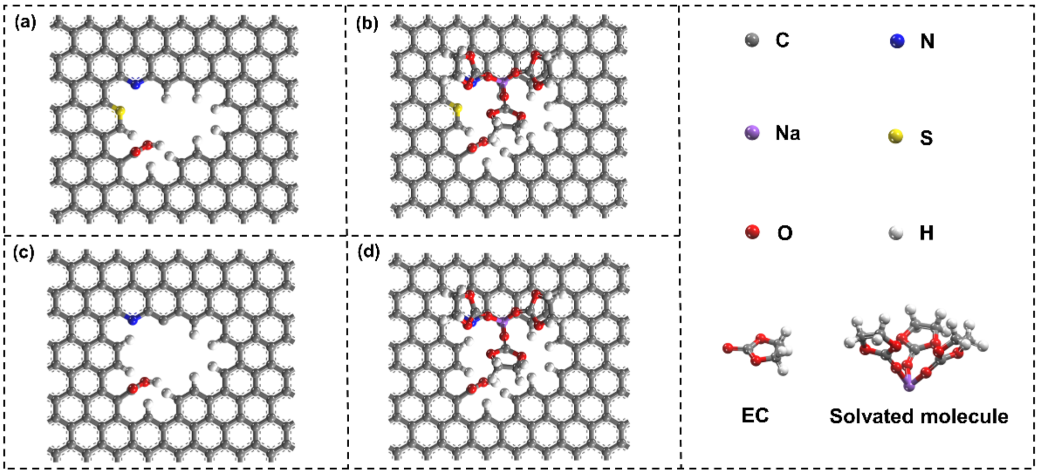

Fig. S7 Model structure showing interactions between solvated molecules and doped carbon: (a, b) N, O, S tri-doping model, (c, d) N, O co-doping model.

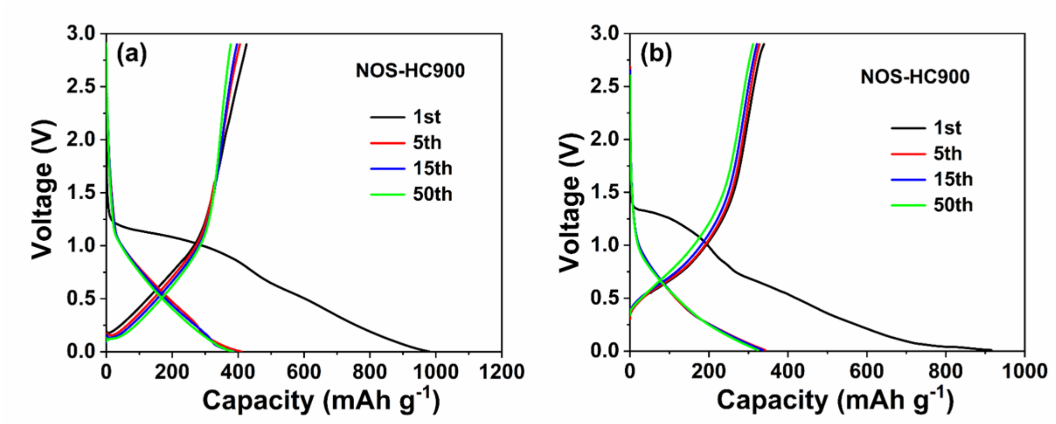

Fig. S8 The GCD profiles from 1st to 500th cycle at 100 mA g^{-1}.

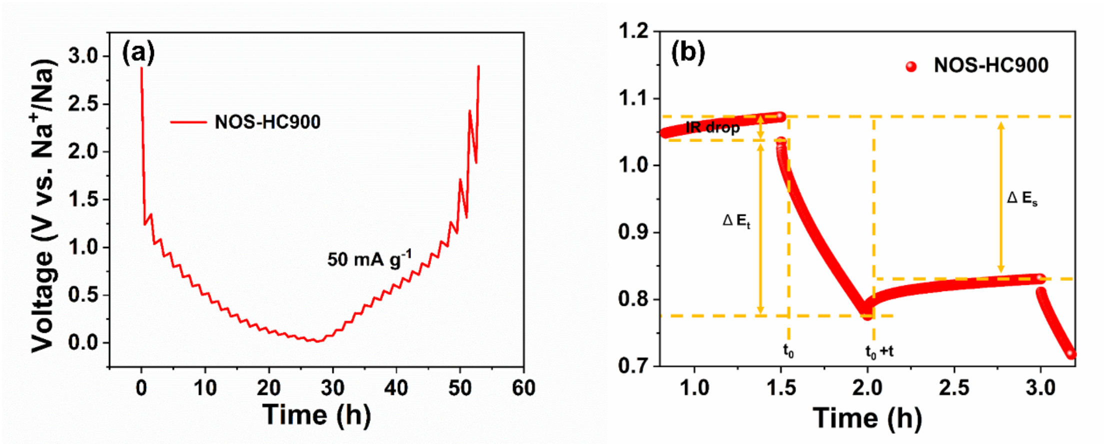

Fig. S9 (a) GITT profile as a function of time during the 300th cycle in the voltage range of 0.01-2.9 V (vs. Na^+/Na) for NOS-HC900. (b) The determination of ΔEτ and ΔEs from the measured GITT profiles.

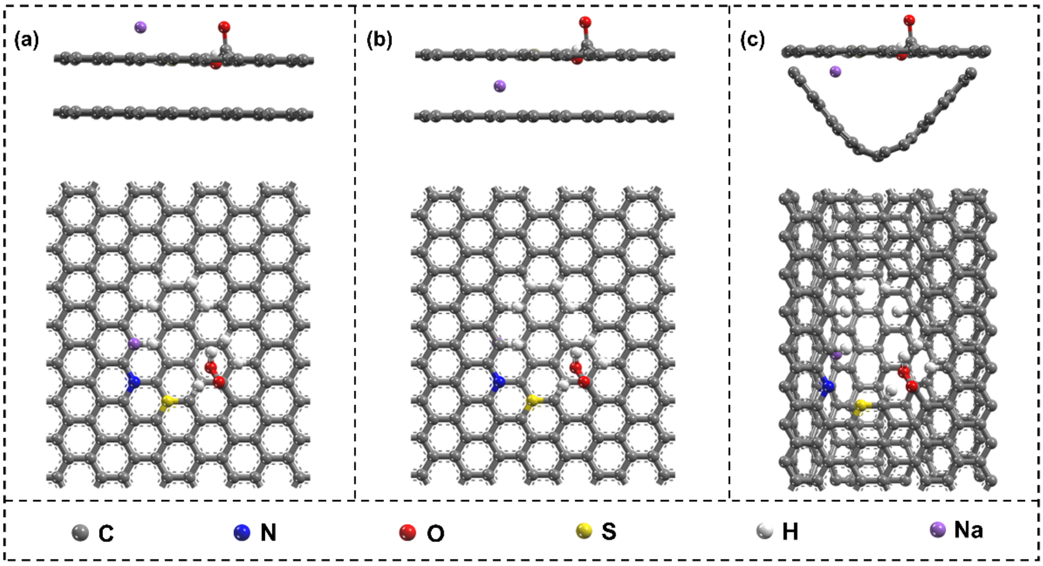

Fig. S10 The stable structures for Na acting on different active sites: (a) adsorption, (b) intercalation and (c) pore-filling.

Table S1 Textural properties of the samples of NOS-HC700, NOS-HC800, NOS-HC900, NOS-HC1000 and NOS-HC1100.

Samples	$d_{(002)}$ (nm)	I_D/I_G	S_{BET} ($m^2\ g^{-1}$)	V_p ($cm^3\ g^{-1}$)
NOS-HCs700	0.371	0.93	60.1	0.45
NOS-HCs800	0.380	0.99	57.7	0.33
NOS-HCs900	0.392	1.02	55.8	0.29
NOS-HCs1000	0.395	1.05	49.9	0.24
NOS-HCs1100	0.401	1.10	45.1	0.18

Table S2 Peak assignment of C 1s, N 1s, O 1s and S 2p for NOS-HC900.

Peak	Binding energy (eV)	Assignment	Fraction of species (%)
C 1s	284.7	C-C/C=C	78.6
	285.3	C-N/C=N	9.8
	285.8	C-O/C=O	7.4
	286.8	C-S	4.2
N 1s	398.5	Pyridinic N	14.1
	400.9	Graphitic N	56.9
	402.7	Pyridine-N	29.0
O 1s	531.8	C=O	18.9
	533.1	O-C-O/C-OH	63.3
	534.6	COOH	17.8
S 2p	164.3	S $2p_{3/2}$: C-S-C	58.1
	165.4	S $2p_{1/2}$: C-S-C	25.4
	168.4	Oxidized sulfur species	16.4

Table S3 Element analysis of samples under different temperatures

Sample	C	H	N	O	S
NOS-HC700	77.18	0.51	8.73	9.51	4.07
NOS-HC800	79.57	0.45	8.84	7.20	3.94
NOS-HC900	81.67	0.32	8.46	5.93	3.62
NOS-HC1000	84.87	0.28	6.95	5.37	2.53
NOS-HC1100	88.69	0.27	4.57	4.49	1.98

The element content is calculated by a mass fraction (wt.%, dry basis).

Table S4 Comparison of the sodium-storage performance for carbon-based anode in the recent literatures with our sample.

Electrode materials	Rate performance Charge (mAh g^{-1}) / Current density (mA g^{-1})	Cycling performance Charge (mAh g^{-1}) / Current density (mA g^{-1}) / Cycles	Ref.
NOS-HC900	**425.3 / 100** **315.1 / 2000**	**402.5 / 100 / 1000**	**Our work**
HC/VC-1300	420 / 50 68 / 1000	261 / 100 /100	[1]
HC-Al_2O_3-5%	321.5 / 50 83.6 / 1000	72.6 / 1000 / 2000	[2]
SHCs-1500	305 / 30	286 / 30 / 300	[3]
CSHP2	250 / 100 123 / 1000	215 / 100 / 100	[4]
PFHC-20	334.3 / 20	196.9 / 100 /300	[5]
NSC2	280 / 50 102 / 10	223 / 1000 / 2000	[6]
NPDCs-700	212 / 2000 150 / 5000	197 / 2000 / 2000	[7]
carbon@750 C	367.6 / 50 65.8 / 5000	161.5 / 2000 / 5000	[8]
SAC-750	67 / 3000	303 / 100/ 100	[9]
HPC-UP-6	416.9 / 50 253.6 / 1000	341.5 / 50 / 100	[10]
BPC-1100	400 / 50 145 / 1000	332.8 / 50 / 400	[11]
HCMT-1300	302 / 100 201 / 1000	301 / 100 / 100	[12]
ENMC	234 / 100 129 / 2000	154 / 1000 / 1000	[13]
WSC-1500	352 / 100 182 / 1000	305 / 100 / 200	[14]
HCS-3	310.5 / 50	266.2 / 100 / 300	[15]

Table S5 Equivalent circuit parameters of the NOS-HC900 for SIBs after cycling.

Type	Cycle number	R_s/Ohm	R_{SEI}/Ohm	R_{ct}/Ohm
SIBs	Pristine	7.8	4.9	158.9
	10^{th} cycle	6.1	10.2	67.5
	50^{th} cycle	6.0	15.3	44.3
	100^{th} cycle	5.9	15.6	42.9
PIBs	Pristine	18.1	82.5	1580.2
	10^{th} cycle	26.3	143.1	837.6
	50^{th} cycle	34.5	154.4	386.3
	100^{th} cycle	48.2	158.1	368.5

Table S6 Comparison of the potassium-storage performance for carbon-based anode in the recent literatures with our sample.

Electrode materials	**Rate performance** Charge (mAh g^{-1}) / Current density (mA g^{-1})	**Cycling performance** Charge (mAh g^{-1}) / Current density (mA g^{-1}) / Cycles	**Ref.**
NOS-HC900	**342.6 / 100** **231.7 / 2000**	**322.7 / 100 / 1000**	**Our work**
HCLP	300 / 50 121 / 2000	211.6 / 50 /200	[16]
MW-HC	321.5 / 50 170 / 200	136 / 200 / 100	[17]
CQDHC	313 / 100	237 / 100 / 150	[18]
NO-YS-CS	473.7 / 20 183.3 / 1000	215 / 500 / 2500	[19]
SHC-3	298.1 / 100	283.8 / 100 /1000	[20]
NSO-HCN	209.6 / 50 136.0 / 500	184.2 / 100 / 200	[21]
I/N-HC	278 / 200 150 / 800	185 / 200 / 400	[22]
PI-T-Pab	200.3 / 50	146.1 / 100 / 100	[23]
CS-1000	298 / 100 262 / 200	217 / 200/ 500	[24]
N-CNC	254.0 / 100 107.9 / 2000	132.9 / 1000 / 200	[25]
PNTCDA@900	220.7 / 100 193.9 / 200	169.0 / 100 / 150	[26]
SPCS	232.6 / 200	165.2 / 1000 / 1500	[27]
N-CLNTs-700	303.4 / 50 266.0 / 100	261.0 / 50 / 150	[28]
NCS-5	302 / 50 280 / 100	205 / 1000 / 2000	[29]
OPDMC	224 / 30	150.3 / 200 / 2000	[30]

Table S7 XPS binding energy values and peak assignment for C 1s.

C 1s	Position (eV)	0 nm	Position (eV)	15 nm	Position (eV)	30 nm	Peak assignment
3th	283.2	18.1%	283.1	16.6%	282.9	30.6%	Na_x-HC
	284.5	29.2%	284.4	14.3%	284.2	43.5%	C-C, C-H
	286.0	35.5%	285.9	33.2%	285.8	11.9%	C-O
	288.6	17.2%	288.5	35.9%	288.5	14.0%	RCO_3
300th	283.5	4.3%	283.0	42.2%	282.9	39.4%	Na_x-HC
	284.5	48.2%	284.2	20.8%	283.9	25.0%	C-C, C-H
	286.0	22.7%	285.7	12.9%	285.5	9.5%	C-O
	288.4	24.8%	288.3	24.1%	288.1	26.1%	RCO_3

References

[1] F. Chen, Y. Di, Q. Su, D. Xu, Y. Zhang, S. Zhou, et al., Vanadium-modified hard carbon spheres with sufficient pseudographitic domains as high-performance anode for sodium-ion batteries, Carbon Energy (2022).

[2] C. Yu, Y. Li, H. Ren, J. Qian, S. Wang, X. Feng, et al., Engineering homotype heterojunctions in hard carbon to induce stable solid electrolyte interfaces for sodium-ion batteries, Carbon Energy (2022).

[3] B. Yang, J. Wang, Y. Zhu, K. Ji, C. Wang, D. Ruan, et al., Engineering hard carbon with high initial coulomb efficiency for practical sodium-ion batteries, J. Power Sources 492 (2021) 229656.

[4] S. Chen, K. Tang, F. Song, Z. Liu, N. Zhang, S. Lan, et al., Porous hard carbon spheres derived from biomass for high-performance sodium/potassium-ion batteries, Nanotechnology 33 (2021) 055401.

[5] G. Zhang, L. Zhang, Q. Ren, L. Yan, F. Zhang, W. Lv, et al., Tailoring a Phenolic Resin Precursor by Facile Pre-oxidation Tactics to Realize a High-Initial-Coulombic-Efficiency Hard Carbon Anode for Sodium-Ion Batteries, ACS Appl. Mater. Inter. 13 (2021) 31650-31659.

[6] Q. Jin, K. Wang, P. Feng, Z. Zhang, S. Cheng, K. Jiang, Surface-dominated storage of heteroatoms-doping hard carbon for sodium-ion batteries, Energy Stor. Mater. 27 (2020) 43-50.

[7] T. Shi, X. Wei, J. Zheng, F. Kong, P. Cui, D. Wu, et al., Soybean Roots-Derived N, P Co-doped Mesoporous Hard Carbon for Boosting Sodium and Potassium-ion Batteries, Carbon 178 (2021) 233-242.

[8] J. Sun, Y. Sun, J.A.S. Oh, Q. Gu, W. Zheng, M. Goh, et al., Insight into the structure-capacity relationship in biomass derived carbon for high-performance sodium-ion batteries, J. Energy Chem. 62 (2021) 497-504.

[9] C. Senthil, J.W. Park, N. Shaji, G.S. Sim, C.W. Lee, Biomass seaweed-derived nitrogen self-doped porous carbon anodes for sodium-ion batteries: Insights into the structure and electrochemical activity, J. Energy Chem. 64 (2022) 286-295.

[10] J. Zhang, D. Zhang, K. Li, Y. Tian, Y. Wang, T. Sun, N, O and S co-doped

hierarchical porous carbon derived from a series of samara for lithium and sodium storage: Insights into surface capacitance and inner diffusion, J. Colloid Interf. Sci. 598 (2021) 250-259.

[11] C. Chen, Y. Huang, Y. Zhu, Z. Zhang, Z. Guang, Z. Meng, et al., Nonignorable influence of oxygen in hard carbon for sodium ion storage, ACS Sustain. Chem. Eng. 8 (2020) 1497-1506.

[12] D. Yang, S. Li, D. Cheng, L. Miao, W. Zhong, X. Yang, et al., Nitrogen, sulfur, and phosphorus codoped hollow carbon microtubes derived from silver willow blossoms as a high-performance anode for sodium-ion batteries, Energ. Fuel. 35 (2021) 2795-2804.

[13] S. Huang, D. Yang, X. Qiu, W. Zhang, Y. Qin, C. Wang, et al., Boosting Surface-Dominated Sodium Storage of Carbon Anode Enabled by Coupling Graphene Nanodomains, Nitrogen-Doping, and Nanoarchitecture Engineering, Adv. Funct. Mater. (2022) 2203279.

[14] Q. Li, Y.N. Zhang, S. Feng, D. Liu, G. Wang, Q. Tan, et al., N, S self-doped porous carbon with enlarged interlayer distance as anode for high performance sodium ion batteries, Int. J. Energ. Res. 45 (2021) 7082-7092.

[15] X. Chen, Y. Fang, H. Lu, H. Li, X. Feng, W. Chen, et al., Microstructure-dependent charge/discharge behaviors of hollow carbon spheres and its implication for sodium storage mechanism on hard carbon anodes, Small 17 (2021) 2102248.

[16] Z. Liu, S. Wu, Y. Song, T. Yang, Z. Ma, X. Tian, et al., Non-negligible Influence of Oxygen in Hard Carbon as an Anode Material for Potassium-Ion Batteries, ACS Appl. Mater. Inter. (2022).

[17] Z. Wu, J. Zou, S. Shabanian, K. Golovin, J. Liu, The roles of electrolyte chemistry in hard carbon anode for potassium-ion batteries, Chem. Eng. J. 427 (2022) 130972.

[18] Y. Guo, Y. Feng, H. Li, Y. Wang, Z. Wen, G. Zhou, Carbon quantum dots in hard carbon: An approach to achieving PIB anodes with high potassium adsorption, Carbon 189 (2022) 142-151.

[19] S. Chong, L. Yuan, T. Li, C. Shu, S. Qiao, S. Dong, et al., Nitrogen and Oxygen

Co-Doped Porous Hard Carbon Nanospheres with Core-Shell Architecture as Anode Materials for Superior Potassium-Ion Storage, Small 18 (2022) 2104296.

[20] X. Chen, X.-B. Cheng, Z. Liu, High sulfur-doped hard carbon anode from polystyrene with enhanced capacity and stability for potassium-ion storage, J. Energy Chem. 68 (2022) 688-698.

[21] M. Chen, Y. Cao, C. Ma, H. Yang, AN/S/O-tridoped hard carbon network anode from mercaptan/polyurethane-acrylate resin for potassium-ion batteries, Nano Energy 81 (2021) 105640.

[22] Y. Zhang, Y. Yang, C. Huang, H. Fan, D. Yuan, W.-B. Luo, et al., Understanding the effect of I/N dual-doped hard carbon for high performance K-ion storage, Electrochim. Acta 394 (2021) 139146.

[23] M. Wang, Y. Zhu, Y. Zhang, T. Yang, J. Duan, C. Wang, Cost-effective hard–soft carbon composite anodes with promising potassium ions storage performance, Electrochim. Acta 368 (2021) 137649.

[24] D. Wang, G. Du, D. Han, Q. Su, S. Ding, M. Zhang, et al., Porous flexible nitrogen-rich carbon membranes derived from chitosan as free-standing anodes for potassium-ion and sodium-ion batteries, Carbon 181 (2021) 1-8.

[25] F. Yuan, H. Sun, D. Zhang, Z. Li, J. Wang, H. Wang, et al., Enhanced electron transfer and ion storage in phosphorus/nitrogen co-doped 3D interconnected carbon nanocage toward potassium-ion battery, J. Colloid Interf. Sci. 611 (2022) 513-522.

[26] Y. Liu, Q. Ru, Y. Gao, Q. An, F. Chen, Z. Shi, et al., Constructing volcanic-like mesoporous hard carbon with fast electrochemical kinetics for potassium-ion batteries and hybrid capacitors, Appl. Surf. Sci. 525 (2020) 146563.

[27] H. Zhang, C. Luo, H. He, H.-H. Wu, L. Zhang, Q. Zhang, et al., Nano-size porous carbon spheres as a high-capacity anode with high initial coulombic efficiency for potassium-ion batteries, Nanoscale horiz. 5 (2020) 895-903.

[28] S. Tian, Y. Wang, T. Cai, D. Kong, D. Wang, H. Ren, et al., Polyaniline-derived carbon nanotubes as anode materials for potassium-ion batteries: insight into the effect of N-doping, Appl. Surf. Sci. 534 (2020) 147635.

[29] Y. Li, K. Xiao, C. Huang, J. Wang, M. Gao, A. Hu, et al., Enhanced potassium-ion storage of the 3d carbon superstructure by manipulating the nitrogen-doped species and morphology, Nano-micro lett. 13 (2021) 1-14.

[30] R. Verma, P.N. Didwal, J.Y. Hwang, C.J.J.B. Park, Supercaps, Recent Progress in Electrolyte Development and Design Strategies for Next-Generation Potassium-Ion Batteries, Batteries Supercaps 4 (2021) 1428-1450.